

# Direct Detection Under Tukey Signalling

Amir Tasbihi *Graduate Student Member, IEEE* and Frank R. Kschischang *Fellow, IEEE*

**Abstract**—A new direct-detection-compatible signalling scheme is proposed for fiber-optic communication over short distances. Controlled inter-symbol interference is exploited to extract phase information, thereby achieving data rates within one bit per channel-use of those of a coherent detector.

**Index Terms**—direct detection, short-haul, ISI, Tukey window

## I. INTRODUCTION

**D**IRECT detection or, synonymously, square-law detection, is a nonlinear waveform detection scheme based upon measuring the squared magnitude of a complex-valued waveform. It appears in various scientific fields, *e.g.*, crystallography [1], radio astronomy [2], [3], biomedical spectroscopy [4], detection and estimation theory [5]–[7], etc. This paper deals with the application of square-law detection in fiber-optic communication systems [8], [9], particularly those with short transmission length, *e.g.*, less than 10 km. Such systems occur, *e.g.*, in rack-to-rack data transmission within data centers.

Since square-law detectors base their decision only on the magnitude of the received complex-valued waveform—unlike coherent detectors which also access phase information—one might get the intuitive (but erroneous) impression that the information rate of a communication channel under square-law detection should be roughly half the information rate of the same channel under coherent detection [10]–[13]. However, it can be shown that the capacity of waveform channels under square-law detection of bandlimited [14] and time-limited [15] signals is, in fact, at most one bit less, per used dimension, than the capacity under coherent detection! Thus, the price to pay for the convenience of direct detection may not be as high as intuition would suggest. Unfortunately, [14] and [15] do not present a practical scheme to achieve the lower bound on the capacity derived in those papers.

Due to the simplicity of direct detection, finding efficient communication schemes compatible with square-law detection has become an intriguing research problem. One popular recent scheme is the *Kramers–Kronig receiver* [16] which has been investigated thoroughly in the optical communication literature in the last few years. The Kramers–Kronig receiver enables recovery of a complex-valued waveform from its squared magnitude, which in turn enables the use of digital signal processors to mitigate dispersion, making direct detection viable for longer transmission lengths ( $> 100$  km) than previously thought, where dispersion is a hindering

factor [17]–[19]. These merits come with drawbacks however: a high required carrier-to-signal power ratio [20] and increased sampling rates necessitated by spectrum-broadening operations performed after the square-law device.

In this paper, a new direct-detection-compatible data transmission scheme is proposed. Unlike typical communication systems, where inter-symbol interference (ISI) is a nuisance, the proposed scheme exploits controlled ISI to extract phase information. As a toy example to illustrate that ISI can be beneficial, suppose that  $z_1$  and  $z_2$  are two complex numbers. Then, from  $|z_1|^2$ ,  $|z_2|^2$ , and  $|z_1 + z_2|^2$  (an ISI term), one can retrieve the phase difference between  $z_1$  and  $z_2$ , up to a sign ambiguity. As another example, let

$$g(t) = \sum_{\ell=0}^m g_{\ell} \operatorname{sinc}(t - \ell),$$

where  $g_0, \dots, g_m \in \mathbb{C}$  and  $\operatorname{sinc}(t) \triangleq \frac{\sin(\pi t)}{\pi t}$ . The goal is to find  $g_0, \dots, g_m$  from samples of  $|g(t)|^2$  at  $t = \frac{k}{2}$ , where  $k = 0, \dots, 2m$ . Since

$$\left| g\left(\frac{k}{2}\right) \right|^2 = \begin{cases} |g_{\frac{k}{2}}|^2, & \text{if } k \text{ is even;} \\ \left| \sum_{\ell=0}^m g_{\ell} \operatorname{sinc}\left(\frac{k}{2} - \ell\right) \right|^2, & \text{if } k \text{ is odd,} \end{cases}$$

one can easily recover the magnitudes of  $g_0, \dots, g_m$  from the samples with an even  $k$ , while their phases are embedded in samples with an odd  $k$ . Unfortunately, since all  $g_{\ell}$ 's contribute to the samples at half-integer times, recovering phase information is an intractable problem, even for moderately small values of  $m$ . Therefore, while ISI is useful to extract phase information, an excessive ISI would demand complex processing. This is the rationale for claiming that “controlled ISI” is needed.

The rest of the paper is organized as follows. The system model, including the transmitter, the channel, and the receiver, is described in Sec. II. In particular, the new signalling scheme is proposed in Sec. II-B. The scheme is validated via numerical simulations, whose results are given in Sec. III. Finally, concluding remarks are provided in Sec. IV.

Throughout this paper, vectors are denoted by lower-case bold letters, *e.g.*,  $\mathbf{v}$ . For a vector  $\mathbf{v}$  of length  $m$ ,  $\mathbf{v}[k]$  denotes its  $k^{\text{th}}$  entry, where  $k \in \{0, \dots, m-1\}$ . The cardinality of a finite set  $\mathcal{A}$  is denoted by  $|\mathcal{A}|$ . The expected value and the variance of a random variable  $X$  are denoted as  $\mathbb{E}[X]$  and  $\operatorname{Var}(X)$ , respectively. Likelihood functions will always be denoted as  $f$ , with arguments chosen to indicate the random variables involved; for example, the conditional probability density function of a random variable  $Y$  at a point  $y \in \mathbb{R}$  given that a random variable  $X$  takes value  $x$  is denoted simply as  $f(y | x)$  rather than the more cumbersome  $f_{Y|X}(y | x)$ . The

Submitted to *J. Lightwave Techn.* on May 26th, 2021. The authors are with the Edward S. Rogers Sr. Dept. of Electrical & Computer Engineering, University of Toronto, Toronto, ON M5S 3G4, Canada. Email: {tasbihi, frank}@ece.utoronto.ca.

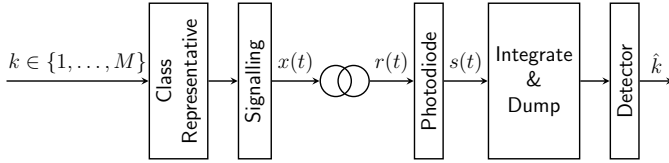


Fig. 1. The system model. We assume that  $r(t) = \rho x(t)$ , where  $\rho \in (0, 1]$ .

notation  $X \sim \mathcal{N}(\mu, \sigma^2)$  indicates that random variable  $X$  has a Gaussian distribution with mean  $\mu$  and variance  $\sigma^2$ . Finally, the set of positive real numbers is denoted as  $\mathbb{R}^{>0}$ .

## II. THE SYSTEM MODEL

In this section we explain the system model, shown in Fig. 1. For simplicity and without loss of generality, we assume a complex baseband model.

### A. The Transmission Medium

As explained in Sec. I, the proposed scheme is aimed at short-range fiber-optic communications, *e.g.*, over a distance  $< 10$  km. Therefore, to avoid amplified spontaneous-emission (ASE) noise, we assume an unamplified optical link. Indeed, we assume that the only source of noise is the photodiode, as discussed in Sec. II-C. We assume transmission at the zero-dispersion wavelength of single-mode optical fibers (SMFs), *i.e.*, about 1310 nm. Zero-dispersion transmission trades off with a non-minimal power loss, which for SMFs is about  $0.5 \text{ dB} \cdot \text{km}^{-1}$ . As a result, the received optical waveform is  $r(t) = \rho x(t)$ , where  $x$  is the transmitted complex-valued waveform and  $\rho \in (0, 1]$  is the loss factor, depending on the fiber length. Through the rest of the paper, and for simplicity in computations, we assume that  $\rho = 1$ , which in optical communications is known as back-to-back transmission. It should be mentioned that the BER and the mutual-information figures, discussed in Sec. III, depend on the received optical-signal power. Thus, for a given non-zero transmission length, *i.e.*, with  $\rho < 1$ , the needed launch power can be computed easily. An example for  $\rho < 1$  is presented in Sec. III.

### B. Tukey Signalling

In this section, we discuss the operation done in the “signalling” unit of Fig. 1, which is the central contribution of this paper. For a positive integer  $n$ , this unit accepts  $n$  complex numbers,  $x_0, \dots, x_{n-1} \in \mathbb{C}$ , called the transmitted symbols, or simply the symbols, at its input. The block outputs the waveform  $x \in \mathbb{C}^{\mathbb{R}}$ , given as

$$x(t) = \sum_{d=0}^{n-1} x_d w(t - dT), \quad (1)$$

where  $T \in \mathbb{R}^{>0}$  is the inverse of the baud rate, and  $w$  is a real-valued signalling waveform. Through the rest of the paper,  $n$  denotes the number of transmitted symbols. Often in communication systems,  $w$  is chosen to be a sinc waveform, a raised-cosine waveform, a root raised-cosine waveform, etc. However, their “ISI patterns” are complicated, *i.e.*, at a given

time  $t$  when the ISI is non-zero, many, if not all, of the transmitted symbols contribute to the squared-magnitude of  $x(t)$ . As explained in Sec. I, this increases the detection complexity. To avoid this, only a few transmitted symbols should interfere at time  $t$ , which is achieved when  $w$  is supported over a relatively short time interval. However, this reduction in the “timewidth” of  $w$  increases its bandwidth. To tackle this issue,  $w$  should have a tapered edge, *i.e.*, it should drop slowly and smoothly toward zero. A familiar function having this behaviour is the Fourier transform of the raised-cosine function. Note, however, that  $w$  must possess this tapering property in the time domain, not in the frequency domain. We propose the use of the following family of waveforms.

For a  $\beta \in [0, 1]$ , let

$$w_\beta(t) \triangleq \begin{cases} \frac{2}{\sqrt{4-\beta}}, & \text{if } |t| \leq \frac{(1-\beta)}{2}; \\ \frac{1}{\sqrt{4-\beta}} \left( 1 - \sin \left( \frac{\pi(2|t|-1)}{2\beta} \right) \right), & \text{if } \left| |t| - \frac{1}{2} \right| \leq \frac{\beta}{2}; \\ 0, & \text{otherwise.} \end{cases} \quad (2)$$

Note that  $w_\beta$  has unit energy, *i.e.*,  $\int_{-\infty}^{\infty} w_\beta^2(t) dt = 1$ , and is supported over a time interval of duration  $1+\beta$ . This waveform is known in spectrum estimation as the *cosine-tapered window* or the *Tukey window*, named after mathematician and founder of “modern spectrum estimation” [21], John W. Tukey, who suggested them as a combination of *rectangular* and *Hann* windows [22]–[24]. Indeed,  $w_0$  and  $w_1$  are rectangular and Hann windows, respectively. To avoid introducing a new name for  $w_\beta$  as a signalling waveform, we refer to it as a *Tukey waveform*. Fig. 2 shows Tukey waveforms for two different  $\beta$  values.

We set  $w$  in (1) to be a dilated Tukey waveform; in particular,  $w(t) = w_\beta(\frac{t}{T})$ . By this choice of  $w$ , at any time  $t$  within the support of  $x$ , either one or two of the transmitted symbols contribute to  $|x(t)|^2$ . This facilitates phase information recovery from the induced ISI. Accordingly we define two types of time intervals, to be used in later sections, as follows. For  $k \in \{0, \dots, n-1\}$ , the waveform  $x$  depends only on  $x_k$  whenever  $|t - kT| \leq \frac{(1-\beta)T}{2}$ . Thus, we define the  $k^{\text{th}}$  ISI-free interval as

$$\mathcal{Y}_k \triangleq \left[ \left( k - \frac{1-\beta}{2} \right) T, \left( k + \frac{1-\beta}{2} \right) T \right]. \quad (3)$$

Similarly, for  $\ell \in \{0, \dots, n-2\}$ ,  $x(t)$  depends on both  $x_\ell$  and  $x_{\ell+1}$  whenever  $|t - (\ell + \frac{1}{2})T| < \frac{1}{2}\beta T$ . Therefore, we define the  $\ell^{\text{th}}$  ISI-present interval as

$$\mathcal{Z}_\ell \triangleq \left( \left( \ell + \frac{1-\beta}{2} \right) T, \left( \ell + \frac{1+\beta}{2} \right) T \right). \quad (4)$$

The ISI-free and ISI-present intervals are shown (for  $n = 3$ ) in Fig. 3.

A concern may arise about the required bandwidth for transmitting  $x$  over the optical fiber. The Fourier transform

TABLE I  
THE FRACTION OF THE TOTAL ENERGY OF  $w_\beta$  WITHIN ITS MAIN SPECTRAL LOBE

| $\beta$ | fraction (%) | $\beta$ | fraction (%) | $\beta$ | fraction (%) |
|---------|--------------|---------|--------------|---------|--------------|
| 0.1     | 92.4         | 0.25    | 95           | 0.5     | 98           |
| 0.75    | 99.5         | 0.8     | 99.7         | 0.9     | 99.9         |

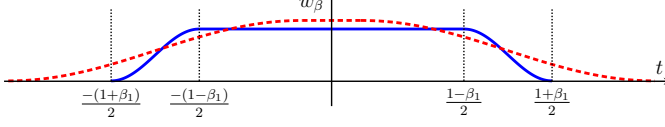


Fig. 2. Tukey waveforms  $w_{\beta_1}$  (solid) and  $w_{\beta_2}$  (dashed);  $\beta_1 < \beta_2$ .

of  $w_\beta$ ,  $W_\beta$ , is

$$W_\beta(f) \triangleq \begin{cases} \frac{\pi}{2\sqrt{4-\beta}} \text{sinc}\left(\frac{1}{2\beta}\right), & \text{if } f = \frac{\pm 1}{2\beta}; \\ \frac{2}{\sqrt{4-\beta}} \text{sinc}(f) \frac{\cos(\pi\beta f)}{1-(2\beta f)^2}, & \text{otherwise.} \end{cases}$$

Fig. 4 shows  $W_\beta$  for two different  $\beta$  values. The fraction of the total energy of  $w_\beta$  contained within the main spectral lobe, i.e.,  $|f| \leq 1$ , is given in Table I. One observes that, although not strictly bandlimited, the bandwidth of  $w_\beta$ , to a good approximation, is unity for large values of  $\beta$ . Furthermore, the numerical simulations in Sec. III support the use of large  $\beta$  values in terms of BER and mutual information.

Note that  $w_\beta$  is not orthogonal to its unit-shift replica, i.e.,  $\int_{-\infty}^{\infty} w_\beta(t)w_\beta(t-1)dt \neq 0$ . This lack of orthogonality must be taken into account when computing the average power of the waveform  $x$ . Luckily, in the case when the symbols are independent and identically distributed (i.i.d.) random variables, Theorem 1 shows that this power is indeed given as the mean squared value of the symbol magnitudes.

**Theorem 1.** For a positive integer  $m$  and  $P \in \mathbb{R}^{>0}$ , let  $\lambda_0, \dots, \lambda_{m-1}$  be i.i.d. zero-mean complex random variables such that  $\mathbb{E}[|\lambda_0|^2] = P$  and  $\text{Var}(|\lambda_0|^2) < \infty$ . Furthermore, let

$$\Lambda_m(t) = \sum_{j=0}^{m-1} \lambda_j w_\beta\left(\frac{t}{T} - j\right).$$

Then,

$$\frac{1}{mT} \int_{-\infty}^{\infty} |\Lambda_m(t)|^2 dt \xrightarrow{P} P \quad \text{as } m \rightarrow \infty,$$

i.e., the power of  $\Lambda_m$  converges to  $P$  in probability.

*Proof:* See Appendix. ■

We remark that finiteness of  $\text{Var}(|\lambda_0|^2)$  is a very mild condition which is true for all finite signal constellations and indeed most of the usual distributions over an infinite range.

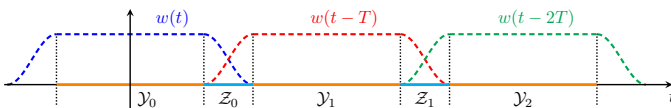


Fig. 3. ISI-free and ISI-present intervals for  $n = 3$ .

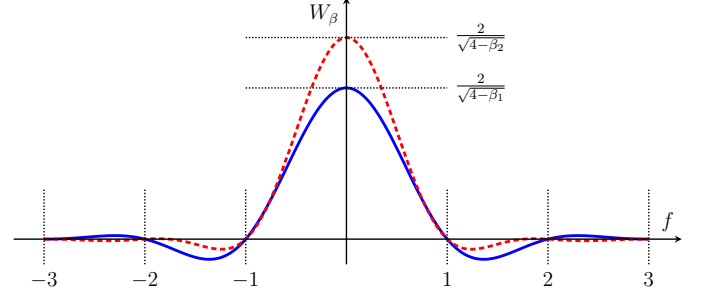


Fig. 4. Fourier transforms of  $w_{\beta_1}$  (solid) and  $w_{\beta_2}$  (dashed);  $\beta_1 < \beta_2$ .

### C. Photodiode, the Noise Source

The received optical waveform,  $r$ , is converted to an electrical signal by a photodiode, which is the only source of noise in this communication scheme. The photodiode has a gain which, for simplicity, is assumed to be unity in this section. However, the actual gain is taken into account in the numerical simulations presented in Sec. III. The output of the photodiode is a real-valued waveform  $s$ , such that

$$s(t) = |r(t)|^2 + |r(t)|n_{\text{sh}}(t) + n_{\text{th}}(t), \quad (5)$$

where  $n_{\text{sh}}(\cdot)$  and  $n_{\text{th}}(\cdot)$  are independent zero-mean white Gaussian random processes with constant two-sided power spectral densities (PSDs)  $\sigma_{\text{sh}}^2$  and  $\sigma_{\text{th}}^2$ , respectively. The  $|r(t)|n_{\text{sh}}(t)$  and  $n_{\text{th}}(t)$  terms are known, respectively, as shot noise and thermal noise [8]. It should be mentioned that photodiodes have additional practical deficiencies, such as, e.g., dark current. However, we assume that such effects contribute negligibly compared to the noise terms in (5).

### D. Integrate & Dump

In this section, we discuss the integrate-and-dump unit in Fig 1. As noted in Sec. II-B, at any time  $t$  within the support of  $x$ , either one or two of the transmitted symbols contribute to  $|x(t)|^2$ . The integrate-and-dump unit integrates its input waveform over each  $\mathcal{Y}_k$  and  $\mathcal{Z}_\ell$  interval, producing  $y_k$  and  $z_\ell$ , respectively, where  $k \in \{0, \dots, n-1\}$  and  $\ell \in \{0, \dots, n-2\}$ . More precisely,

$$y_k \triangleq \int_{\mathcal{Y}_k} s(t) dt, \quad (6)$$

and

$$z_\ell \triangleq \int_{\mathcal{Z}_\ell} s(t) dt. \quad (7)$$

We expand (6) as follows. Let  $\alpha \triangleq \frac{2}{\sqrt{4-\beta}}$ ; then, by using  $r(t) = x(t)$  (see Sec. II-A), we get

$$y_k = \alpha^2(1-\beta)T|x_k|^2 + \alpha|x_k|n_k + m_k, \quad (8)$$

where

$$n_k \triangleq \int_{\mathcal{Y}_k} n_{\text{sh}}(t) dt \sim \mathcal{N}(0, \sigma_{\text{sh}}^2(1-\beta)T),$$

and

$$m_k \triangleq \int_{\mathcal{Y}_k} n_{\text{th}}(t) dt \sim \mathcal{N}(0, \sigma_{\text{th}}^2(1-\beta)T).$$

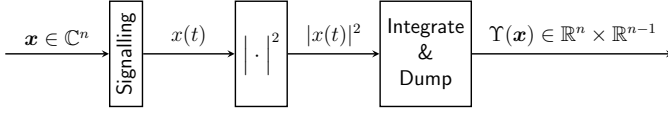


Fig. 5. The  $\Upsilon$  function maps the input of the signalling block to the corresponding output of the integrate-and-dump block in the absence of noise. The noisy photodiode of Fig. 1 has been replaced with an ideal  $|\cdot|^2$  block.

Note that  $\mathbb{E}[n_k n_{k'}] = \mathbb{E}[m_k m_{k'}] = 0$ , for any  $k' \neq k$ , where  $k' \in \{0, \dots, n-1\}$ .

We expand (7) as follows. Let  $\psi : \mathbb{C}^2 \rightarrow \mathbb{R}$  be defined as

$$\psi(v, w) = \frac{1}{4}|v + w|^2 + \frac{1}{8}|v - w|^2,$$

for any  $v$  and  $w \in \mathbb{C}$ . Then, (7) can be simplified as

$$z_\ell = \alpha^2 \beta T \psi(x_\ell, x_{\ell+1}) + \alpha \sqrt{\psi(x_\ell, x_{\ell+1})} p_\ell + q_\ell, \quad (9)$$

where  $p_\ell \sim \mathcal{N}(0, \beta T \sigma_{\text{sh}}^2)$ , and  $q_\ell \sim \mathcal{N}(0, \beta T \sigma_{\text{th}}^2)$ . Similarly,  $\mathbb{E}[p_\ell p_{\ell'}] = \mathbb{E}[q_\ell q_{\ell'}] = 0$ , for any  $\ell' \neq \ell$ . Note that for any  $k$  and  $k' \in \{0, \dots, n-1\}$  and for any  $\ell$  and  $\ell' \in \{0, \dots, n-2\}$ , the four random variables  $n_k, m_{k'}, p_\ell$ , and  $q_{\ell'}$  are mutually independent.

### E. Equivalence Classes

In this section, we discuss the first unit in Fig. 1, *i.e.*, choice of class representative. Let  $\Upsilon : \mathbb{C}^n \rightarrow \mathbb{R}^n \times \mathbb{R}^{n-1}$  denote the function that maps a vector  $\mathbf{x} = (x_0, \dots, x_{n-1}) \in \mathbb{C}^n$  as the input of the signalling block to the corresponding output of the integrate-and-dump block in the absence of noise, as shown in Fig. 5. Specifically, if  $x(t) = \sum_{d=0}^{n-1} x_d w(t-dT)$  then  $\Upsilon(\mathbf{x}) = (\mathbf{y}, \mathbf{z})$ , where  $\mathbf{y} \in \mathbb{R}^n$  is such that

$$\mathbf{y}[k] = \int_{\mathcal{Y}_k} |x(t)|^2 dt,$$

for  $k \in \{0, \dots, n-1\}$ , and  $\mathbf{z} \in \mathbb{R}^{n-1}$  is such that

$$\mathbf{z}[\ell] = \int_{\mathcal{Z}_\ell} |x(t)|^2 dt,$$

for  $\ell \in \{0, \dots, n-2\}$ .

We define an equivalence relation on  $\mathbb{C}^n$  as follows. Two vectors  $\mathbf{x}$  and  $\tilde{\mathbf{x}} \in \mathbb{C}^n$  are said to be *square-law identical*, denoted  $\mathbf{x} \equiv \tilde{\mathbf{x}}$ , if and only if  $\Upsilon(\mathbf{x}) = \Upsilon(\tilde{\mathbf{x}})$ . If  $\mathbf{x}$  and  $\tilde{\mathbf{x}}$  are not square-law identical, they are said to be *square-law distinct*, denoted  $\mathbf{x} \not\equiv \tilde{\mathbf{x}}$ . Since the relation  $\equiv$  is indeed an equivalence relation, it partitions  $\mathbb{C}^n$  into disjoint equivalence classes.

For any positive integer  $M$ , let  $\mathcal{S}$  be a set of cardinality  $M$ , whose elements are complex-valued vectors of length  $n$ , called *symbol blocks*, which are square-law distinct. In other words,  $\mathcal{S} = \{\mathbf{x}_1, \dots, \mathbf{x}_M\} \subset \mathbb{C}^n$  such that  $\mathbf{x}_k \not\equiv \mathbf{x}_\ell$  if  $k \neq \ell$ . Then, the class-representative unit outputs the symbol block  $\mathbf{x}_k$  if its input is  $k \in \{1, \dots, M\}$ . Note that the entries of symbol blocks are in fact the transmitted symbols. Furthermore, note that the information rate of this communication scheme cannot exceed  $\frac{1}{n} \log_2(M)$  bit/sec/Hz.

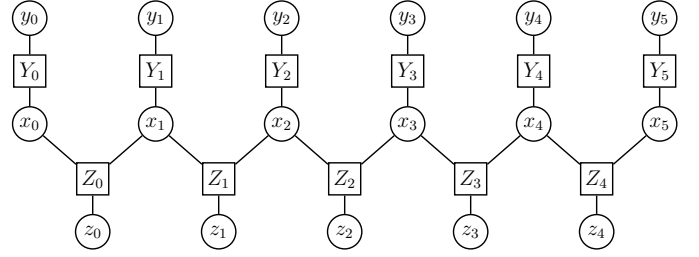


Fig. 6. The factor graph of the ML block detection for  $n = 6$ . For  $k \in \{0, \dots, 5\}$ , the  $Y_k$  factor node represents  $f(y_k | x_k)$ . Similarly, for  $\ell \in \{0, \dots, 4\}$ , the  $Z_\ell$  factor node represents  $f(z_\ell | x_\ell, x_{\ell+1})$ .

### F. Maximum-Likelihood Block Detection

In this section, we discuss the last unit in Fig. 1, namely, the detector. In practice, the choice of detection rule and its algorithm will depend on hardware limitations and performance requirements. Through out this paper, maximum-likelihood (ML) block detection is chosen as the detection rule. In other words, if  $\mathbf{y} = (y_0, \dots, y_{n-1})$  and  $\mathbf{z} = (z_0, \dots, z_{n-2})$  are the buffered outputs of the integrate-and-dump unit, the detector chooses  $\hat{k} \in \{1, \dots, M\}$  as the transmitted index if and only if

$$\hat{k} = \arg \max_{d \in \{1, \dots, M\}} f(\mathbf{y}, \mathbf{z} | \mathbf{x}_d).$$

For any  $k \in \{0, \dots, n-1\}$ , (8) implies that, given  $x_k$ ,

$$y_k \sim \mathcal{N}\left(\alpha^2(1-\beta)T|x_k|^2, (1-\beta)T(\alpha^2|x_k|^2\sigma_{\text{sh}}^2 + \sigma_{\text{th}}^2)\right). \quad (10)$$

Furthermore, for any  $\ell \in \{0, \dots, n-2\}$ , (9) implies that, given  $x_\ell$  and  $x_{\ell+1}$ ,

$$z_\ell \sim \mathcal{N}\left(\alpha^2 \beta T \psi(x_\ell, x_{\ell+1}), \beta T(\alpha^2 \psi(x_\ell, x_{\ell+1})\sigma_{\text{sh}}^2 + \sigma_{\text{th}}^2)\right). \quad (11)$$

Thus,

$$\begin{aligned} f(\mathbf{y}, \mathbf{z} | \mathbf{x}_d) &= f(\mathbf{y} | \mathbf{x}_d) f(\mathbf{z} | \mathbf{x}_d) \\ &= \prod_{k=0}^{n-1} f(y_k | \mathbf{x}_d[k]) \prod_{\ell=0}^{n-2} f(z_\ell | \mathbf{x}_d[\ell], \mathbf{x}_d[\ell+1]), \end{aligned} \quad (12)$$

where  $f(y_k | \mathbf{x}_d[k])$  and  $f(z_\ell | \mathbf{x}_d[\ell], \mathbf{x}_d[\ell+1])$  can be computed from (10) and (11), respectively. Fig. 6 is the factor-graph representation [25] of (12). Note that the variances of  $y_k$  and  $z_\ell$ , given in (10) and (11), are functions of the transmitted symbols; therefore, minimum Euclidean-distance detection is not equivalent to ML block detection.

## III. NUMERICAL SIMULATION

In this section, the communication scheme proposed in Sec. II is verified by numerical simulations.

### A. The Photodiode

We assume the use of an InGaAs avalanche photodiode (APD), as among different types of APDs, these have high

TABLE II  
PARAMETER VALUES USED IN THE NUMERICAL SIMULATION

| Parameter                                  | Value       | Typical Range (InGaAs APD)            |
|--|-------------|---------------------------------------|
| Temperature ( $T_k$ )                      | 300 K       |                                       |
| Load Resistance ( $R_L$ )                  | 15 $\Omega$ |                                       |
| APD Gain ( $M_{APD}$ )                     | 20          | 10 – 40                               |
| Enhanced Responsivity ( $M_{APD}R_{APD}$ ) | 10 mA/mW    | 5 – 20                                |
| $k$ -factor ( $k_{APD}$ )                  | 0.6         | 0.5 – 0.7                             |
| Excess Noise Factor ( $F$ )                | 12.78       | a function of $M_{APD}$ and $k_{APD}$ |

bandwidth. In this case, the two-sided PSD of the thermal noise,  $n_{th}(\cdot)$ , is [8]

$$\sigma_{th}^2 = \frac{2kT_k}{R_L},$$

where  $k$  is the Boltzmann constant,  $T_k$  is the temperature, and  $R_L$  is the external load resistance. Furthermore, for the received optical complex-valued waveform  $r$ , the shot noise is  $|r(t)|n_{sh}(t)$  where the two-sided PSD of  $n_{sh}(\cdot)$  is

$$\sigma_{sh}^2 = eM_{APD}^2FR_{APD},$$

where  $e$  is the unit charge,  $M_{APD}$  is the APD gain,  $F$  is the excess noise factor, and  $R_{APD}$  is the responsivity of APD. Table II gives the values for these parameters used in simulations.

### B. The Transmitter Symbols

The transmitted symbols are chosen from a finite constellation,  $\mathcal{K}$ , three of which are shown in Fig. 7. Indeed,  $\mathcal{S} \subset \mathcal{K}^n$ , and since the symbol blocks must be square-law distinct, there is a loss in the maximum achievable rate in the proposed scheme, compared to its coherent-detection counterpart. Table III provides the number of equivalent classes of each possible size for different values of  $n$ , and for 2-ring/4-ary phase constellation (see Fig. 7b). For example, for  $n = 4$  there are 432 equivalence classes, among which 192 have size 8. As there are  $|\mathcal{K}|^n = 8^4$  possible vectors of length 4 over  $\mathcal{K}$ , the lost rate is  $\frac{1}{4} \log_2 \left( \frac{8^4}{432} \right) = 0.94$  bits per channel-use (c.u.). Table III shows that the larger is  $n$ , the smaller is the rate loss. However, this reduction in rate loss comes with a higher detection complexity. Specifically, the number of equivalence classes grows exponentially with  $n$ , which itself increases the complexity of the ML block decoder.

It should be noted that a relatively small  $n$  suffices to achieve a practical target BER. This is because the transmission scheme is usually the inner-most layer of a larger communication system, which typically also employs an outer error-correcting code.

### C. Mutual Information

Fig. 8 shows the achievable rate per channel-use in different scenarios, plotted against the received optical power (ROP), computed by a Monte Carlo method. In Figs. 8(a)–8(e), the transmitted symbol block is chosen independently and uniformly among all symbol blocks, *i.e.*, class representatives.

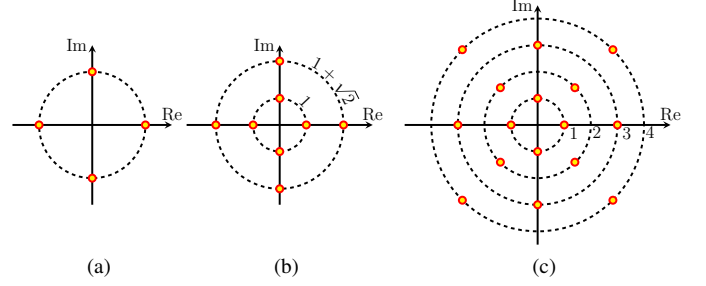


Fig. 7. Three choices for  $\mathcal{K}$ , the constellation from which the transmitted symbols come: (a) 4-PSK (phase shift keying), (b) 2-ring/4-ary phase, and (c) 4 ring/4-ary phase constellations. The ratio of the outer-ring radius to the inner one in (b) is  $1 + \sqrt{2}$ . In (c), the rings are equi-spaced.

TABLE III  
NUMBER OF CLASSES FOR EACH CLASS SIZE FOR 2-RING/4-ARY PHASE CONSTELLATION

| class size \ $n$   | 3    | 4    | 5    | 6     | 7     |
|--|------|------|------|-------|-------|
| 4  | 32   | 128  | 512  | 2048  | 8192  |
| 8  | 32   | 192  | 1024 | 5120  | 24576 |
| 16   | 8    | 96   | 768  | 5120  | 30720 |
| 32   |      | 16   | 256  | 2560  | 20480 |
| 64   |      |      | 32   | 640   | 7680  |
| 128  |      |      |      | 64    | 1536  |
| 256  |      |      |      |       | 128   |
| Total  | 72   | 432  | 2592 | 15552 | 93312 |
| Rate loss (bits/c.u.)  | 0.94 | 0.81 | 0.73 | 0.68  | 0.64  |
| $\frac{1}{n} \log_2 \left( \frac{8^n}{\text{Total}} \right)$ |      |      |      |       |       |

In Fig. 8(f), instead of square-law distinct symbol blocks, all possible vectors of  $\mathcal{K}^n$  have been chosen with uniform distribution. As equivalence classes have different cardinalities (see Table III), a uniform distribution over  $\mathcal{K}^n$  implies a non-uniform distribution over equivalence-class representatives, which gives rise to a huge loss in the achievable rate compared to Figs. 8(a)–8(e). Thus it is important that the transmitted symbol blocks are chosen to be square-law distinct.

As shown in Figs. 8(a)–8(d), the value of  $\beta$  affects the minimum required power to achieve a target data rate, for a fixed constellation  $\mathcal{K}$ . We find that  $\beta = 0.9$  either outperforms other choices of  $\beta$  at close-to-saturation data rates, or the loss is negligible compared to other values of  $\beta$ .

Inspired by [26], Fig. 8(e) shows the mutual information for different constellations and with different values of  $n$ , all with  $\beta = 0.9$ . This figure can be interpreted in two different ways, as follows. First, by fixing the ROP at a constant value, we can achieve a higher data rate by choosing a larger constellation. For example, at the ROP of  $-16$  dBm and with  $n = 3$ , a data rate of 2 bits/c.u. is achievable with the 2-ring/4-ary phase constellation, while a data rate of 2.7 bits/c.u. is achievable with the 4-ring/4-ary phase constellation. Secondly, by selecting a larger  $\mathcal{K}$ , a target data rate is achievable at a smaller ROP. For example, the data rate of 2 bits/c.u. is achievable by the 2-ring/4-ary phase constellation with  $n = 4$  at an ROP  $\simeq -19$  dBm, while by using the 4-ring/4-ary phase constellation, with  $n = 3$  and a channel code of rate  $\simeq 0.7$ , the same data rate is achievable at the ROP of  $-24$  dBm, *i.e.*, with approximately a 5 dB gain. Note that the number of

equivalence classes in the former is 432, while in the latter it is 400; therefore, their ML block-detection complexities are roughly the same.

As discussed earlier in this section, for a fixed constellation  $\mathcal{K}$ , the achievable rate will increase with increasing  $n$ . This fact can be seen from Fig. 8(e). For example, while the maximum achievable rate for 4-ring/4-ary phase constellation is 2.88 bits/c.u. for  $n = 3$ , the maximum achievable rate is 2.99 bits/c.u. and 3.08 bits/c.u. for  $n = 4$  and  $n = 5$ , respectively. Note that the maximum rate for this constellation is 4 bits/c.u. under coherent detection; therefore, in the last case, *i.e.*,  $n = 5$ , the rate is within the bounds given in [14], [15]. Furthermore, although the achievable rates for  $n = 3$  and  $n = 4$  are below the rate lower-bound *i.e.*, 3 bits per c.u., the gap is small, *i.e.*, less than 4% and 0.34%, respectively. The maximum achievable rates for other constellations in Fig. 8(e) are all within one bit of coherent detection.

#### D. Bit Error Rate

Fig. 9 shows the bit error rate of the proposed scheme, for several  $\mathcal{K}$ ,  $\beta$ , and  $n$ . In each scenario,  $M$  is chosen to be an integer power of 2. For example, while there are 432 equivalence classes for the 2-ring/4-ary phase constellation with  $n = 4$ , only  $M = 2^8$  of them are chosen as the symbol blocks, *i.e.*, members of  $\mathcal{S}$ . Furthermore, the  $M$  symbol blocks are randomly mapped to  $M$  bit streams, each of length  $\log_2(M)$ , *i.e.*, no particular labelling algorithm, *e.g.*, Gray code, is being used.

As shown in Fig. 9(a), for the 2-ring/4-ary phase constellation, the BER decreases when increasing  $\beta$  from 0.3 to 0.99. It might be perceived from this figure that a larger value of  $\beta$  results in a better BER performance; therefore, the best BER performance is achieved for the maximum possible value for  $\beta$ , *i.e.*, unity. However, Fig. 9(b) refutes this claim. As shown in this figure, for close-to-unity values of  $\beta$ , a small  $\beta$  increment results in a significant performance loss, in terms of BER. In the extreme case, *i.e.*,  $\beta = 1$ , there is no ISI-free sample, and the  $n$  complex-valued transmitted symbols must be detected from the  $n - 1$  real-valued ISI-present received samples. Thus, there is a significant performance loss, both in terms of BER and the maximum achievable rate.

The BER performance under 4-PSK and 4-ring/4-ary phase constellations are shown in Fig. 9(c) and Fig. 9(d), respectively. In both cases, the performance is improved by increasing  $\beta$  from 0.1 toward 0.9.

Despite the fact that  $\beta = 0.99$  has the best BER performance in Fig. 9(a) for the 2-ring/4-ary phase constellation, because of the discussed high sensitivity of performance to the value of  $\beta$  for  $\beta > 0.99$ ,  $\beta = 0.9$  is used to compare the BER of different constellations in Fig. 9(e). For the purpose of fairness, the horizontal axis is normalized to information rate. Similar to a typical communication over an additive white Gaussian noise (AWGN) channel, for a fixed noise power and at high signal powers, using a larger constellation results in a higher BER; however, at low ROPs, the BER performance is a complicated function of the received power.

The choice of  $\mathcal{K}$  has a big impact on the performance of the proposed scheme. For example, while 16-QAM (quadrature

amplitude modulation) is a typical constellation in communication over AWGN channels, it has poor performance in the proposed scheme, as shown in Fig. 9(f).

#### E. Power & Power Spectral Density

If the transmitted symbols are i.i.d., Theorem 1 guarantees that the average power of the transmitted waveform is equal, in probability, to the variance of those symbols. On the other hand, in Sec. III-C it was noted that uniform selection of symbol blocks from the entire  $\mathcal{K}^n$  results in a significant loss in achievable rate, and therefore must be avoided. Constraining symbol blocks to be square-law distinct makes the transmitted symbols dependent, and thus Theorem 1 does not apply. However, in the numerical simulations it turned out that the average power of the transmitted waveform is equal to  $\mathcal{P}_S$  in all cases studied, where  $\mathcal{P}_S \triangleq \frac{1}{Mn} \sum_{j=1}^M \|x_j\|^2$  is the average power of  $\mathcal{S}$  and where  $\|\cdot\|$  denotes the  $L^2$ -norm.

Table I was used to claim that for large values of  $\beta$ ,  $w_\beta$  has unit bandwidth, to within a good approximation. However, one must be careful to take into account the ISI-present sections of  $x$ , which may cause bandwidth-broadening. This issue is addressed in Fig. 10, which shows the PSD of the transmitted waveform,  $x$ , under 2-ring/4-ary phase constellation. As shown, the larger the value of  $\beta$ , the larger the gap between the main and the second spectral lobe becomes. Specifically, for  $\beta = 0.9$ , the second spectral lobe is 27 dB below the main lobe. This shows that not only does  $\beta = 0.9$  result in a better performance in terms of achievable rate and BER, but it also results in better energy concentration within the main spectral lobe of  $x$ , compared to smaller values of  $\beta$ .

#### F. Comparison With Other Schemes

Due to the difference in channel models, particularly the idealization of optical fibers, a fair comparison of the proposed scheme with other existing schemes is difficult. For example, while we have assumed that there are no optical amplifiers, and, as a result, no ASE noise in the channel, many papers in the literature use erbium-doped fiber amplifiers, which are sources of ASE noise.

Although unfair, to make a comparison, assume the proposed scheme is used to transmit data over a span of 10 km of SMF. The resulting power loss at 1310 nm is 5 dB. By considering an additional 5 dB loss due to other factors, *e.g.*, connector losses and code operation at some gap to the Shannon limit, assume the launch power is 10 dB larger than the received power. Therefore, using Fig. 8(e), we can achieve an information rate of 2 bits per c.u. with the proposed scheme, by using the 4-ring/4-ary phase constellation with  $n = 4$  and a channel code of rate  $2/3$ , at a launch power of  $-14.5$  dBm.

Using a Kramers–Kronig receiver, the authors of [19] achieve a data rate of 4 bits per c.u. at a launch power of 2 dBm. Under the rule of thumb that each additional 3 dB launch power yields an extra bit per symbol in AWGN channels, the scheme of [19] can achieve 2 bits per c.u. at a launch power of about  $-4$  dBm. However, as noted, the channel model of [19] is quite different.

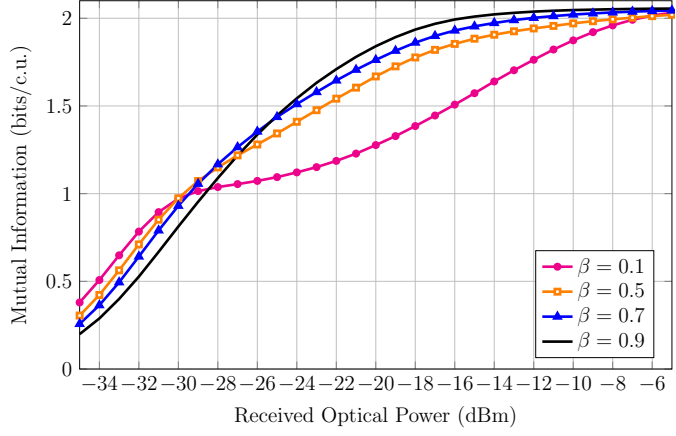
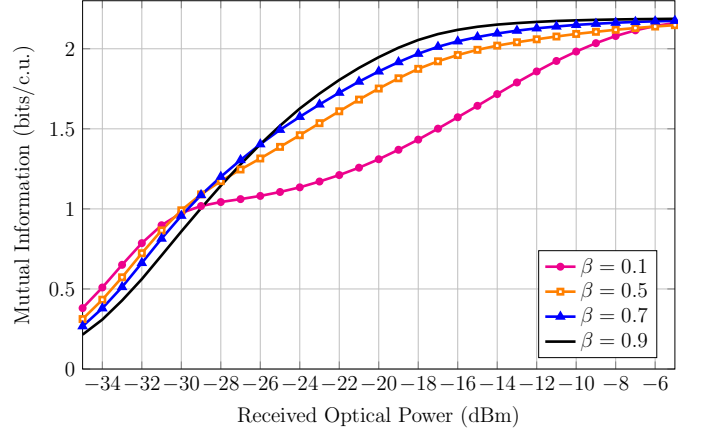
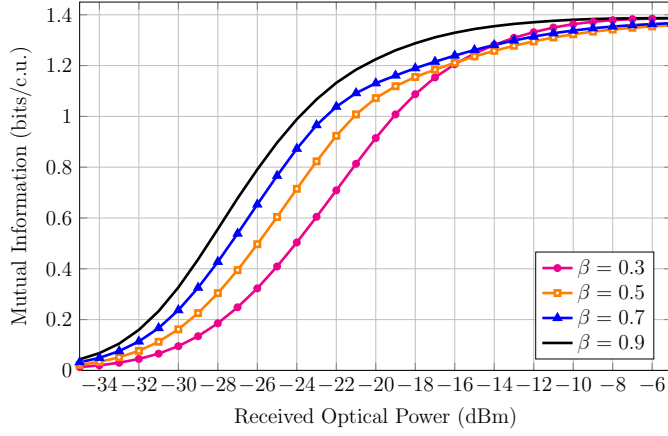
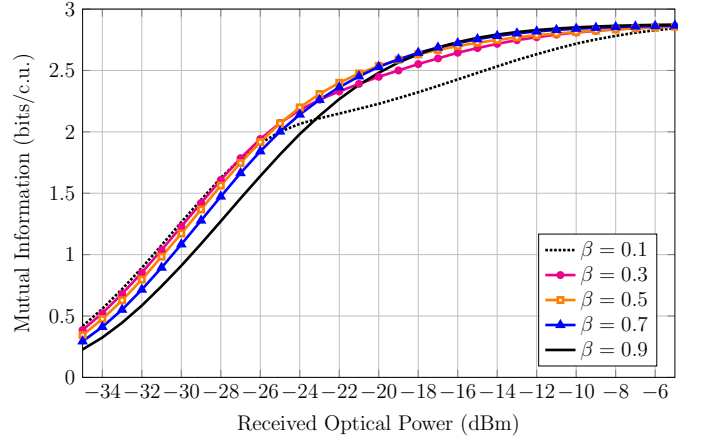
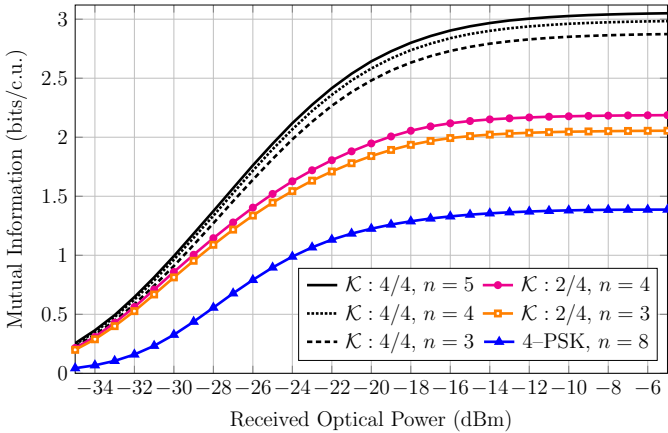
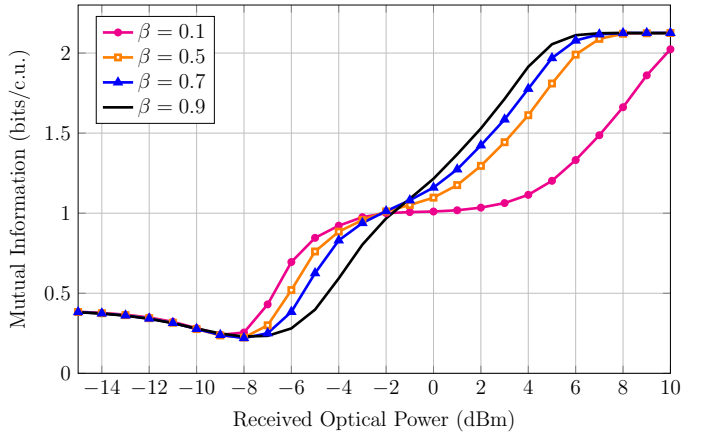
(a)  $\mathcal{K}$  : 2-ring/4-ary phase constellation,  $n = 3$ (b)  $\mathcal{K}$  : 2-ring/4-ary phase constellation,  $n = 4$ (c)  $\mathcal{K}$  : 4-PSK,  $n = 8$ (d)  $\mathcal{K}$  : 4-ring/4-ary phase constellation,  $n = 3$ (e) Uniform input distribution over all equivalence classes,  $\beta = 0.9$ (f) Uniform input distribution over  $\mathcal{K}^4$ ,  $\mathcal{K}$  : 2-ring/4-ary phase constellation

Fig. 8. Mutual information in different scenarios. In (a)–(e) the input distribution is uniform over all equivalence classes, while in (f) the input distribution is uniform over  $\mathcal{K}^4$ , where  $\mathcal{K}$  is the 2-ring/4-ary phase constellation. In part (e),  $\mathcal{K} : a/b$  means that  $\mathcal{K}$  is an  $a$ -ring/ $b$ -ary phase constellation.

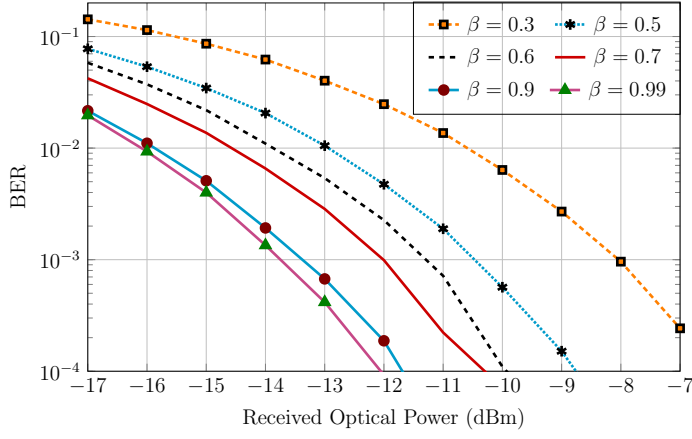
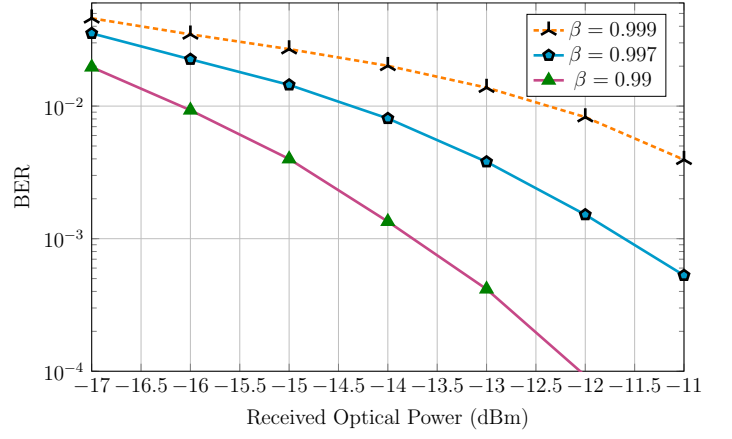
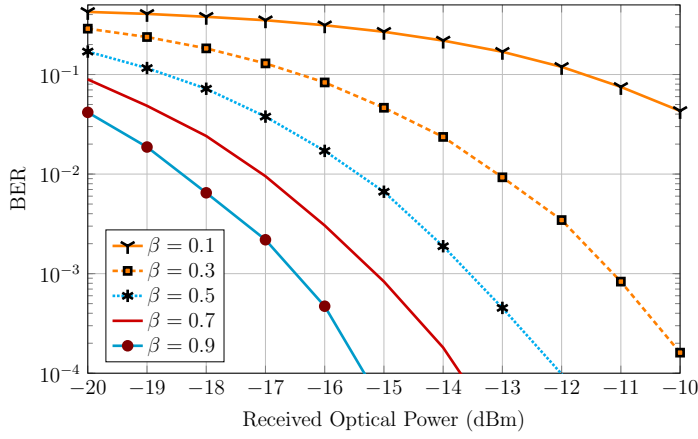
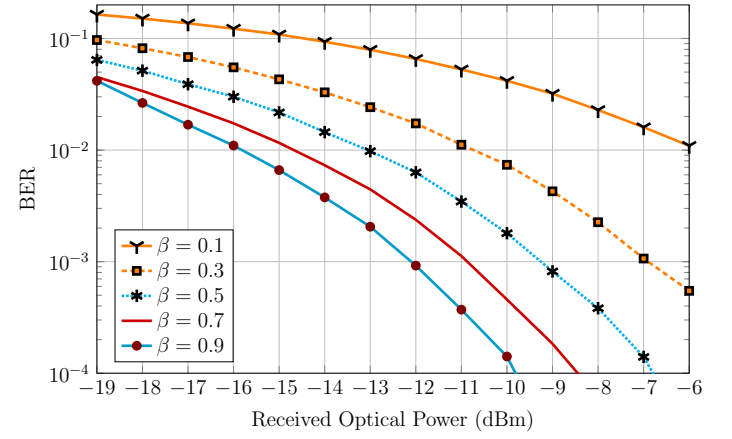
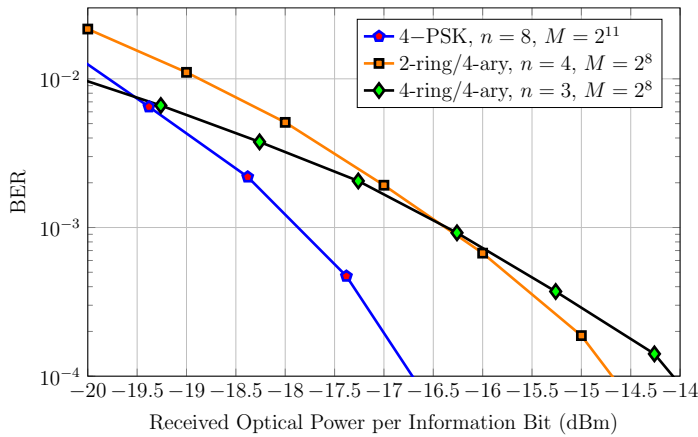
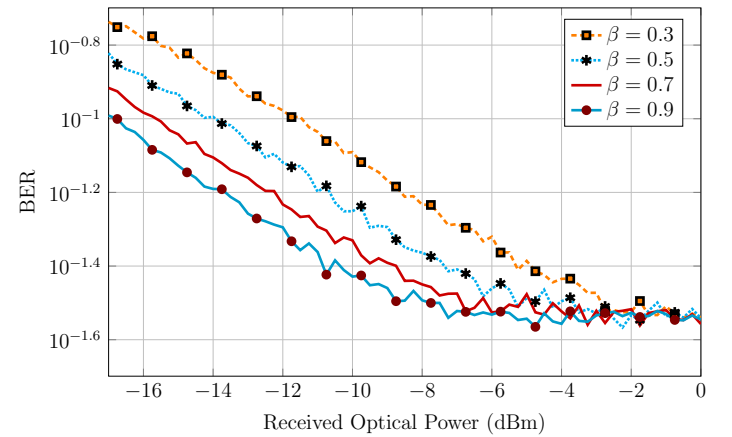
(a)  $\mathcal{K}$  : 2-ring/4-ary phase constellation,  $n = 4$ ,  $M = 2^8$ (b)  $\mathcal{K}$  : 2-ring/4-ary phase constellation,  $n = 4$ ,  $M = 2^8$ (c)  $\mathcal{K}$  : 4-PSK,  $n = 8$ ,  $M = 2^{11}$ (d)  $\mathcal{K}$  : 4-ring/4-ary phase constellation,  $n = 3$ ,  $M = 2^8$ (e) Different constellations with  $\beta = 0.9$ (f)  $\mathcal{K}$  : 16-QAM,  $n = 3$ ,  $M = 2^8$ 

Fig. 9. Bit error rate in different scenarios. Part (f) suggests that the conventional 16-QAM constellation does not have a good performance under the proposed communication scheme.



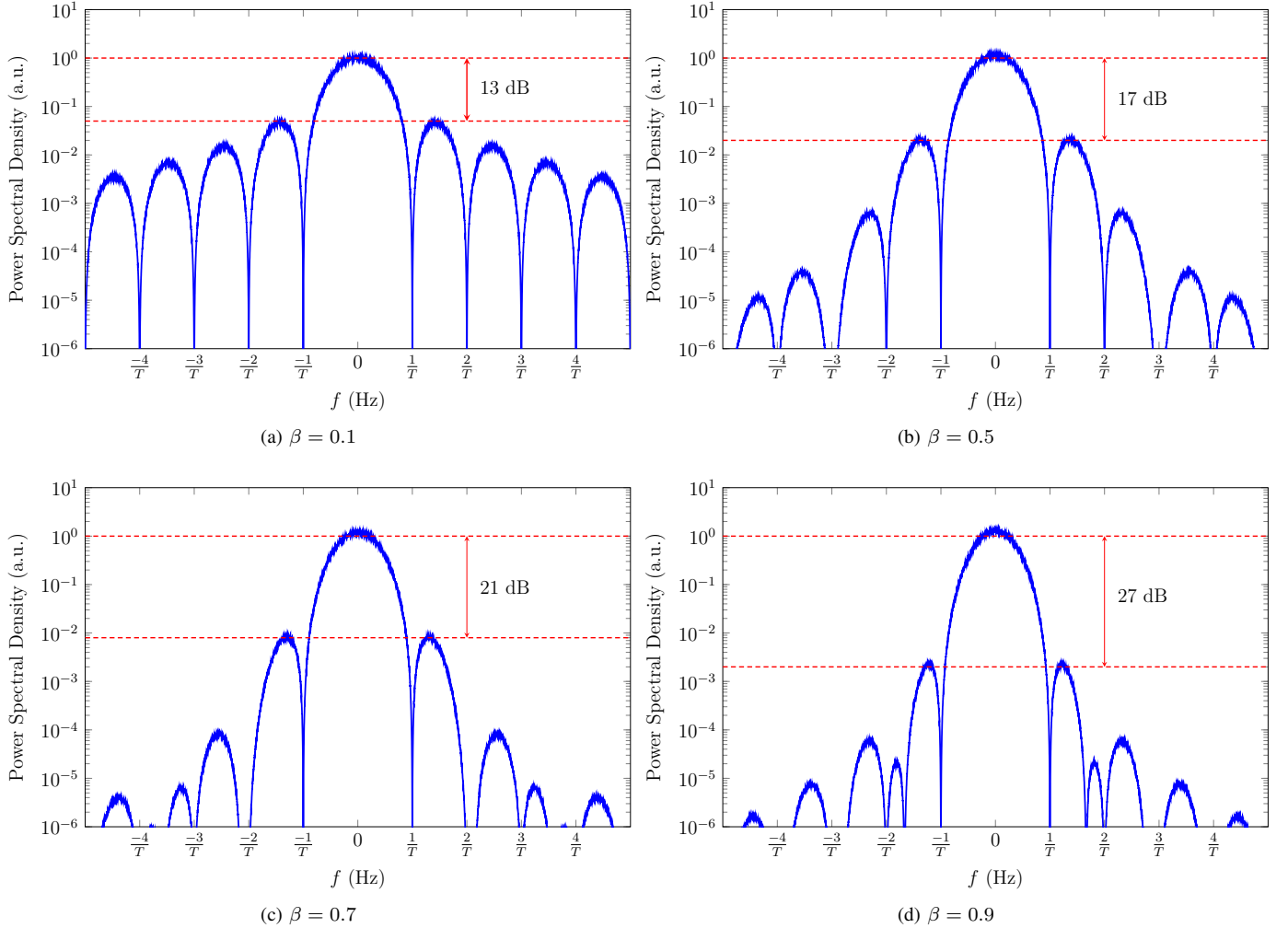


Fig. 10. Power spectral density of the transmitted waveform in arbitrary unit (a.u.) versus frequency, under 2-ring/4-ary phase constellation.

#### IV. DISCUSSION

As well stated by Tukey, “the test of a good procedure is how well it works, not how well it is understood” [27]. So far the proposed scheme has been tested only with computer simulations. It would be interesting to investigate its performance in a practical experiment.

Throughout this paper, we have assumed an unamplified optical link and therefore no ASE noise in the system. It would be interesting to investigate the performance of the proposed scheme in the presence of ASE noise.

We have used maximum-likelihood block detection to detect the transmitted symbol block. It would be intriguing to investigate other detection strategies. For example, we have assumed that blocks are transmitted without guard time, which means that the last symbol of one block interferes with the first symbol of the next block. While our block detection rule ignores the signal received during these intervals of overlap, a sequence-oriented detection algorithm could potentially exploit them.

As noted in Sec. II-F, unlike AWGN channels, Euclidean distance is not an appropriate metric for detecting the transmitted symbol block. It would be interesting to derive an

appropriate metric for the proposed scheme. In addition to giving an insight on detection, such a metric might simplify the detector’s implementation.

We have used only three different constellations to derive the results in this paper, namely, the 2-ring/4-ary phase, the 4-ring/4-ary phase, and the 4-PSK constellations. Furthermore, we showed that 16-QAM gives poor performance. Constellation design is thus another interesting research topic that can be addressed in future works. In particular, given a set of performance criteria, it would be interesting to find the “best” constellation that satisfies the conditions. This question is closely related to the question about metrics, since for a given power, the performance of a constellation improves by increasing the minimum distance between its points.

We did not impose any criterion for choosing equivalence-class representatives, *i.e.*, symbol blocks. It would be interesting to see if some particular elements are better than others to be chosen as class representatives.

Although the numerical simulations revealed that the average transmitter power equals  $\mathcal{P}_S$  in the simulations, it would be interesting to generalize Theorem 1 to allow for dependent symbols. Strengthening the convergence type is

another relevant problem.

No doubt many further interesting problems can be posed.

#### APPENDIX PROOF OF THEOREM 1

For  $k \in \{0, \dots, m-1\}$  and  $\ell \in \{0, \dots, m-2\}$ , let the ISI-free interval  $\mathcal{Y}_k$  and the ISI-present interval  $\mathcal{Z}_\ell$  be as given in (3) and (4), respectively. Then,

$$\frac{1}{T} \int_{-\infty}^{\infty} |\Lambda_m(t)|^2 dt = \sum_{k=0}^{m-1} G_k + \sum_{\ell=0}^{m-2} H_\ell + \zeta_m, \quad (13)$$

where  $G_k \triangleq \frac{1}{T} \int_{\mathcal{Y}_k} |\Lambda_m(t)|^2 dt$ ,  $H_\ell \triangleq \frac{1}{T} \int_{\mathcal{Z}_\ell} |\Lambda_m(t)|^2 dt$ , and

$$\zeta_m = \frac{1}{T} \int_{-\infty}^0 |\Lambda_m(t)|^2 dt + \frac{1}{T} \int_{(m-\frac{1+\beta}{2})T}^{\infty} |\Lambda_m(t)|^2 dt.$$

One may see that  $\mathbb{E}[G_k] = \frac{4(1-\beta)}{4-\beta} P$  and  $\mathbb{E}[H_\ell] = \frac{3\beta}{4-\beta} P$ .

Let  $\bar{G}_m$  and  $\bar{H}_{m-1}$  denote, respectively, the sample average of  $G_k$  and  $H_\ell$  random variables, i.e.,  $\bar{G}_m = \frac{1}{m} \sum_{k=0}^{m-1} G_k$  and  $\bar{H}_{m-1} = \frac{1}{m-1} \sum_{\ell=0}^{m-2} H_\ell$ . Then, (13) implies that

$$\frac{1}{mT} \int_{-\infty}^{\infty} |\Lambda_m(t)|^2 dt = \bar{G}_m + \frac{m-1}{m} \bar{H}_{m-1} + \frac{\zeta_m}{m}. \quad (14)$$

As  $\lambda_k$ 's are i.i.d. for  $k \in \{0, \dots, m-1\}$ , the  $G_k$  random variables are i.i.d. and have finite variance, where the latter is true as  $\text{Var}(|\lambda_k|^2) < \infty$ . As a result, by the weak law of large numbers,

$$\bar{G}_m \xrightarrow{P} \frac{4(1-\beta)}{4-\beta} P \quad \text{as } m \rightarrow \infty. \quad (15)$$

Unlike  $G_k$ 's, the  $H_\ell$  random variables,  $\ell \in \{0, \dots, m-2\}$ , are dependent. However, the dependency is only between adjacent  $H_\ell$ 's. In particular,  $H_i$  and  $H_j$  are dependent, thus,  $\text{Cov}(H_i, H_j) > 0$ , only if  $|i-j| \leq 1$ , where  $i$  and  $j \in \{0, \dots, m-2\}$  and  $\text{Cov}(\cdot, \cdot)$  denotes the covariance. Furthermore, as  $\text{Var}(|\lambda_k|^2) < \infty$  for all  $k \in \{0, \dots, m-1\}$ , it implies that  $\text{Cov}(H_i, H_j) < \infty$ . Therefore,

$$\text{Var}(\bar{H}_{m-1}) = \frac{\sum_{i,j=0}^{m-2} \text{Cov}(H_i, H_j)}{(m-1)^2} = \mathcal{O}\left(\frac{1}{m}\right).$$

Therefore,  $\lim_{m \rightarrow \infty} \text{Var}(\bar{H}_{m-1}) = 0$ , and Chebyshev's inequality implies that

$$\bar{H}_{m-1} \xrightarrow{P} \frac{3\beta}{4-\beta} P \quad \text{as } m \rightarrow \infty. \quad (16)$$

Furthermore,  $\text{Var}\left(\frac{\zeta_m}{m}\right) = \mathcal{O}\left(\frac{1}{m^2}\right)$ ; thus,

$$\frac{\zeta_m}{m} \xrightarrow{P} 0 \quad \text{as } m \rightarrow \infty. \quad (17)$$

As a result, (14), (15), (16), and (17) imply that

$$\frac{1}{mT} \int_{-\infty}^{\infty} |\Lambda_m(t)|^2 dt \xrightarrow{P} P \quad \text{as } m \rightarrow \infty.$$

#### REFERENCES

- [1] C. Giacovazzo, *Phasing in Crystallography: A Modern Perspective*, 1st ed. London, UK: Oxford Univ. Press, 2014.
- [2] B. F. Burke and F. Graham-Smith, *An Introduction to Radio Astronomy*, 3rd ed. Cambridge, UK: Cambridge Univ. Press, 2009.
- [3] J. Aparici, "A wide dynamic range square-law diode detector (for radioastronomy)," *IEEE Trans. Instrum. Meas.*, vol. 37, no. 3, pp. 429–433, Sep. 1988.
- [4] G. E. Nilsson, T. Tenland, and P. Oberg, "A new instrument for continuous measurement of tissue blood flow by light beating spectroscopy," *IEEE Trans. Biomed. Eng.*, vol. BME-27, no. 1, pp. 12–19, Jan. 1980.
- [5] F. F. Digham, M. Alouini, and M. K. Simon, "On the energy detection of unknown signals over fading channels," *IEEE Trans. Commun.*, vol. 55, no. 1, pp. 21–24, Jan. 2007.
- [6] D. R. Hummels, C. Adams, and B. K. Harms, "Filter selection for receivers using square-law detection," *IEEE Trans. Aerosp. Electron. Syst.*, vol. AES-19, no. 6, pp. 871–883, Nov. 1983.
- [7] B. Xu and M. Brandt-Pearce, "Multiuser detection for square-law receiver under Gaussian channel noise with applications to fiber-optic communications," *IEEE Trans. Inf. Theory*, vol. 51, no. 7, pp. 2657–2664, Jul. 2005.
- [8] G. P. Agrawal, *Fiber-Optic Communication Systems*, 4th ed. NJ, USA: John Wiley & Sons, 2010.
- [9] S. Kumar and M. J. Deen, *Fiber Optic Communications: Fundamentals and Applications*, 1st ed. UK: John Wiley & Sons, 2014.
- [10] A. Mecozzi and M. Shtaiif, "On the capacity of intensity modulated systems using optical amplifiers," *IEEE Photon. Technol. Lett.*, vol. 13, no. 9, pp. 1029–1031, Sep. 2001.
- [11] M. I. Yousefi and F. R. Kschischang, "The per-sample capacity of zero-dispersion optical fibers," in *12th Can. Workshop Inf. Theory*, Kelowna, BC, Canada, May 2011, pp. 98–101.
- [12] K. S. Turitsyn, S. A. Derevyanko, I. V. Yurkevich, and S. K. Turitsyn, "Information capacity of optical fiber channels with zero average dispersion," *Phys. Rev. Lett.*, vol. 91, no. 20, p. 203901, Nov. 2003.
- [13] I. Jacobs, "Limits on the power and spectral efficiency of direct detection systems with optical amplifiers," in *35th Asimolar Conf. Signals Syst. Comput.*, Pacific Grove, CA, USA, Nov. 2001, pp. 8–12.
- [14] A. Mecozzi and M. Shtaiif, "Information capacity of direct detection optical transmission systems," *J. Lightwave Techn.*, vol. 36, no. 3, pp. 689–694, Feb. 2018.
- [15] A. Tasbihi and F. R. Kschischang, "On the capacity of waveform channels under square-law detection of time-limited signals," *IEEE Trans. Info. Theory*, vol. 66, no. 11, pp. 6682–6687, Nov. 2020.
- [16] A. Mecozzi, C. Antonelli, and M. Shtaiif, "Kramers-Kronig coherent receiver," *Optica*, vol. 3, no. 11, pp. 1220–1227, 2016.
- [17] Z. Li *et al.*, "SSBI mitigation and the Kramers-Kronig scheme in single-sideband direct-detection transmission with receiver-based electronic dispersion compensation," *J. Lightwave Techn.*, vol. 35, no. 10, pp. 1887–1893, May 2017.
- [18] X. Chen *et al.*, "218-Gb/s single-wavelength, single-polarization, single-photodiode transmission over 125-km of standard singlemode fiber using Kramers-Kronig detection," in *Proc. Opt. Fiber Commun. Conf. Expo. (OFC)*, Los Angeles, CA, USA, Mar. 2017, pp. Th5B.6:1–3.
- [19] —, "Kramers-Kronig receivers for 100-km datacenter interconnects," *J. Lightwave Techn.*, vol. 36, no. 1, pp. 79–89, Jan. 2018.
- [20] Z. Li *et al.*, "Joint optimisation of resampling rate and carrier-to-signal power ratio in direct-detection Kramers-Kronig receivers," in *Eur. Conf. Opt. Commun. (ECOC)*, Gothenburg, Sweden, Sep. 2017, pp. 1–3.
- [21] E. A. Robinson, "A historical perspective of spectrum estimation," *Proc. IEEE*, vol. 70, no. 9, pp. 885–907, Sep. 1982.
- [22] J. W. Tukey, "An introduction to the calculations of numerical spectrum analysis," in *Spectral Analysis of Time Series*, B. Harris, Ed. New York, USA: John Wiley & Sons, 1967, pp. 25–46.
- [23] N. Geckinli and D. Yavuz, "Some novel windows and a concise tutorial comparison of window families," *IEEE Trans. Acoust., Speech, Signal Process.*, vol. 26, no. 6, pp. 501–507, Dec. 1978.
- [24] F. J. Harris, "On the use of windows for harmonic analysis with the discrete Fourier transform," *Proc. IEEE*, vol. 66, no. 1, pp. 51–83, Jan. 1978.
- [25] F. R. Kschischang, B. J. Frey, and H. A. Loeliger, "Factor graphs and the sum-product algorithm," *IEEE Trans. Info. Theory*, vol. 47, no. 2, pp. 498–519, Feb. 2001.
- [26] G. Ungerboeck, "Channel coding with multilevel/phase signals," *IEEE Trans. Inf. Theory*, vol. 28, no. 1, pp. 55–67, Jan. 1982.
- [27] D. R. Brillinger, "John W. Tukey: his life and professional contributions," *Ann. Statist.*, vol. 30, no. 6, pp. 1535–1575, Dec. 2002.